Red-Emitting $SrGa_2O_4:Cu^{2+}$ Phosphor with Super-Long Persistent Luminescence

Wang, Lei; Wang, Cailu; Chen, Yang; Jiang, Yang; Chen, Lei; Xu, Jinzhang; Qu, Bingyan; Hintzen, Hubertus T.

DOI
10.1021/acs.chemmater.2c02748

Publication date
2022

Document Version
Final published version

Published in
Chemistry of Materials

CHEMISTRY OF MATERIALS

pubs.acs.org/cm

Article

Red-Emitting $SrGa_2O_4:Cu^{2+}$ Phosphor with Super-Long Persistent Luminescence

Lei Wang, Cailu Wang, Yang Chen, Yang Jiang, Lei Chen, Jinzhang Xu, Bingyan Qu,* and Hubertus T. Hintzen*

Cite This: *Chem. Mater.* 2022, 34, 10068−10076

Read Online

ACCESS | Metrics & More | Article Recommendations | Supporting Information

ABSTRACT: The red afterglow of current rare-earth-activated long persistent luminescence (LPL) phosphors is largely still less than 6 h, in contrast to the 20 or 30 h long blue- or green-emitting ones, becoming the main obstacle to realize their multiscenario applications in practice. Herein, we report a rare-earth-free red-emitting LPL phosphor $SrGa_2O_4:Cu^{2+}$ that can exhibit an afterglow at about 622 nm lasting over 30 h, which can largely match with the luminance of current blue- or green-emitting LPL phosphors. We find that the Cu^{2+} ion could be charged by ultraviolet light from 280 to 420 nm, and the emission has a very broad band with a full width at half-maximum of about 150 nm. Combining the thermoluminescence measurement and the first-principles calculation, we find that the O vacancies and the −1 charged Ga vacancies could store the holes and contribute to the LPL of $SrGa_2O_4:Cu^{2+}$. Our results may dramatically promote and expand its potential applications and stimulate the research of the multicolor LPL phosphors in future.

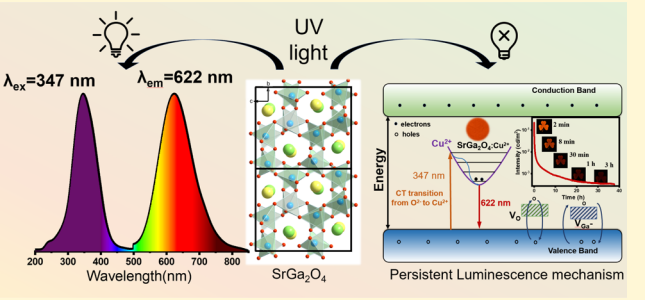

1. INTRODUCTION

The long persistent luminescent (LPL) materials, with outstanding potential applications in optical information storage,[1−3] night vision materials,[4,5] in vivo bioimaging,[6−8] and so forth, have attracted numerous attention because of their unique property of long-lasting emission after the removal of the excitation source. For example, $CaAl_2O_4:Eu^{2+}$, Nd^{3+}[9] exhibits a blue afterglow for more than 19 h, and $SrAl_2O_4:Eu^{2+}$, Dy^{3+}[10] can emit green light, with the afterglow lasting longer than 30 h. However, as one of the RGB color-components, a red emission LPL material is still scarce with a matching afterglow to green and blue in the past 20 years. For example, the present widely used red-emitting LPL materials, such as $Y_2O_2S:Eu^{3+}$, Mg^{2+}, Ti^{4+},[11] and $(Ca_{1-x}, Sr)S:Eu^{2+}$,[12] last typically less than 6 h, which is much shorter than the blue or green LPL materials. Therefore, for a multicolor LPL phosphor design, it is very crucial to explore a new efficient eye-sensitive red-emitting LPL material with a longer decay time to realize promising multiscenario applications in future.

Generally, lanthanide ions are commonly regarded as pivot activators to engineer the luminescence properties of the commercial LPL materials mentioned above. On the contrary, effective 3d transition-metal ion-doped LPL materials, especially with a red emission and a decay time matchable with commercial phosphors, have not been reported so far. Furthermore, the sensitivity of the rare earth price to the global consumption amount greatly limits their applications. Therefore, finding an efficient and lanthanide-ion-free new red-emitting LPL phosphor has been an important and long-standing issue.

As a typical 3d transition-metal ion, Cu^{2+} could show infrared emission in $YGaO_3$,[13] $CaSi_4O_{10}$,[14] $BaSi_4O_{10}$,[15] $Ca_{10}(PO_4)_6(OH)_2$,[16] and $KZnF_3$;[17] orange (599 nm) emission in $SrZrO_3$;[18] and green emission in CaF_2.[19] Hence, it is possible to engineer the luminescent transition of Cu^{2+} by adjusting the type of hosts to achieve its multicolor emissions.

Among the prototypes of AB_2O_4 material, $SrGa_2O_4$ attracts us as it is one of the compounds with a compact structure and wide band gap, for example, which has played essential roles in photoluminescent materials, as it is doped with luminescent centers, such as Eu^{3+}, Ce^{3+}, Tb^{3+}, Cr^{3+}, or Bi^{3+}.[20−25] Specially, the undoped $SrGa_2O_4$ itself is an LPL material, with the afterglow duration time of about 3 min, implying that some trap levels already existing in the host have the capability to delay the emission. Thus, it is feasible to achieve the LPL phenomenon in $SrGa_2O_4$ doped by Cu^{2+}, which is not verified, and the relevant luminescence properties have not been reported before.

Received: September 7, 2022
Revised: October 25, 2022
Published: November 7, 2022

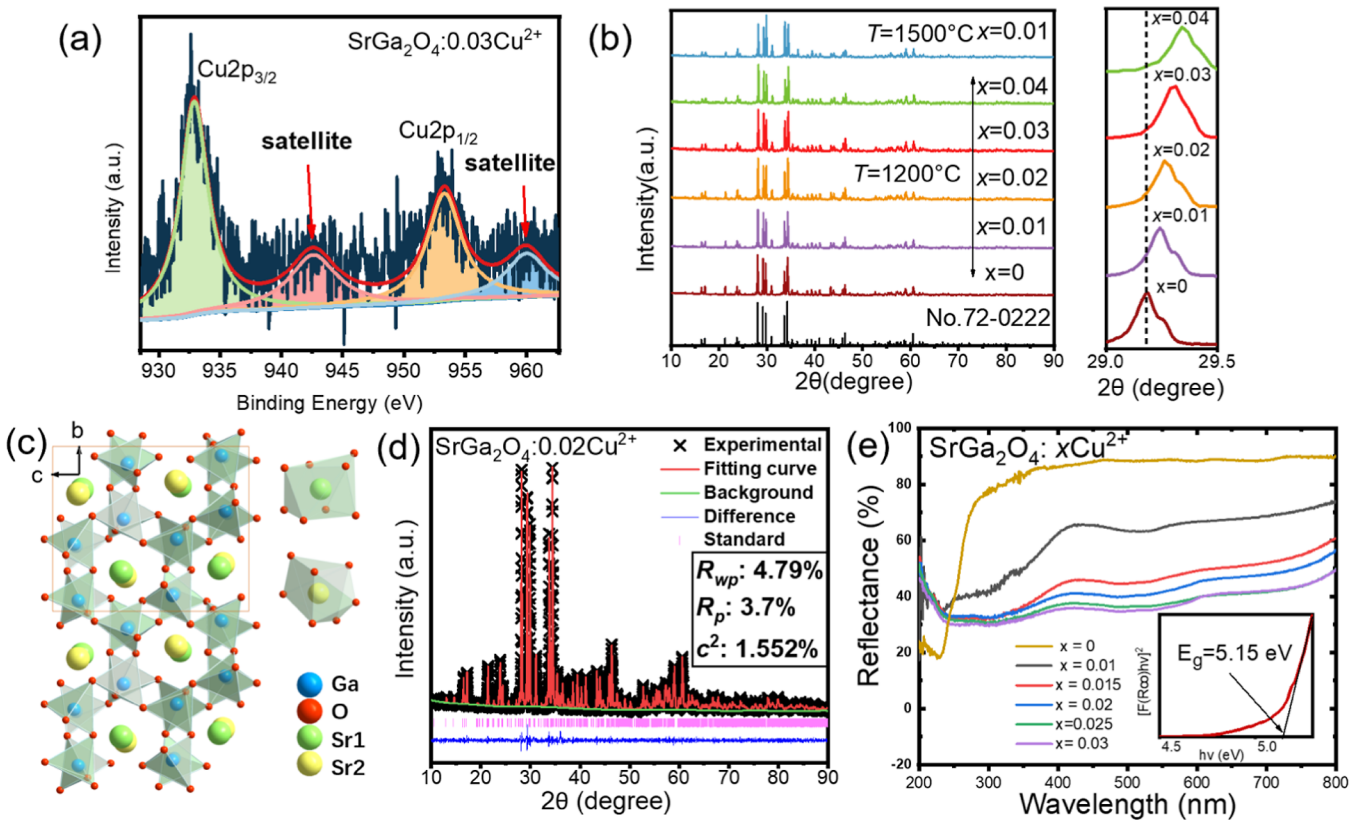

Figure 1. (a) Cu 2p XPS spectrum for the $SrGa_2O_4$:0.03Cu^{2+} sample. (b) XRD patterns of $Sr_{1-x}Ga_2O_4$:xCu^{2+} (x = 0, 0.01, 0.02, 0.03, and 0.04) samples sintered at 1200 °C, $SrGa_2O_4$:0.01Cu^{2+} samples sintered at 1500 °C, and the ICSD no. 72-0222 of $SrGa_2O_4$. The enlarged XRD peak within the range of 29−29.5° is shown on the right-hand side. (c) Schematic crystal structure of $SrGa_2O_4$. (d) Refined XRD pattern of $SrGa_2O_4$:0.02Cu^{2+} sintered at 1200 °C. (e) DRS spectra of $SrGa_2O_4$:xCu^{2+} as a function of Cu concentration x. The inset shows the relationship of $[F(R_\infty)h\nu]^\alpha$ vs $h\nu$ of $SrGa_2O_4$, and here, α = 2 as $SrGa_2O_4$ is a direct gap insulator, as predicted by the first-principles calculation (Figure 2b).

In this work, a series of $Sr_{1-x}Ga_2O_4$:xCu^{2+} (x = 0.01, 0.015, 0.02, 0.025, 0.03, 0.035, and 0.04) phosphors were prepared by the high-temperature solid-state reaction. We found that phosphor could give a red emission, with the maximum at about 622 nm, and the afterglow could last 30 h, compatible to those commercial blue and green LPL materials reported in the literature. The LPL mechanism was studied by the thermoluminescence (TL) spectra and the first-principles calculation, from which we found that the O vacancies and the −1 charged Ga vacancies in the host could play a key role in delaying the emission of Cu^{2+}. As Cu^{2+}-doped LPL materials are relatively scarce, our findings here could inspire more research works on the development of new Cu^{2+} ion-doped phosphors.

2. EXPERIMENTAL METHODS

2.1. Sample Preparation. In this work, $Sr_{1-x}Ga_2O_4$:xCu^{2+} (x = 0, 0.01, 0.015, 0.02, 0.025, 0.03, 0.035, and 0.04) were synthesized by the high-temperature solid-state reaction method. The starting materials $SrCO_3$ (99.95%), Ga_2O_3 (99.99%), and CuO (99.99%) were weighed according to the stoichiometric amounts and ground thoroughly with anhydrous ethanol for 30 min in an agate mortar. The mixed powders were put into corundum crucibles and sintered for 6 h in a high-temperature furnace at 1200, 1350, and 1500 °C, respectively, in air. After cooling to ambient temperature, the as-obtained samples were ground into powder for subsequent analysis and characterization. All the experimental results are collected from the powder samples sintered at 1200 °C except where otherwise denoted.

Part of the as-obtained powder samples was pressed into pellet-like shapes with diameters of 28 mm using a hydraulic press. The pellet-like samples were then sintered for another 6 h at 1200, 1350, and 1500 °C, respectively, in air.

2.2. Characterization. X-ray diffraction (XRD) analysis was characterized by a D/Max 2500V type powder X-ray diffractometer at a scanning step size of 0.02° in the 2θ region from 10 to 90° with a counting time of 0.15 s per step. The Rietveld crystal structure refinement was performed using General Structure Analysis System (GSAS) software. Diffuse reflectance spectroscopy (DRS) spectra were collected in the range of 200−800 nm by a UV/visible spectrometer (Agilent Cary-5000). X-ray photoelectron spectroscopy (XPS) measurements were performed on an ESCALAB 250Xi Thermo Scientific system. The peak shift of binding energy was corrected by using the C 1s (284.8 eV) peak as a reference. The excitation, emission, and afterglow spectra were recorded with a Hitachi F-4600 fluorescence spectrophotometer (scanning speed of 240 nm/min; operating voltage of 400 V). Luminescence decay curves were measured with a Horiba JY Fluorolog-3-tau steady-state/lifetime spectrofluorometer. The TL curves were collected on a FJ-427A1 TL equipment (Beijing Nuclear Instrument Factory). The weight of the measured phosphors was taken constant (0.0020 g). Prior to the TL measurement, the samples were initially exposed to a 365 nm lamp with the power of 8 watts for 30 min and then heated from ambient temperature to 600 K with different rates from 1 to 5 K/s. The LPL lifetime curves were measured with a PR305 long afterglow instrument (Zheda Sensing Company) after the samples were exposed to the same lamp for about 30 min. All the LPL photographs were taken by a digital camera made by Nikon D7500.

2.3. Calculation Method. Both the structure optimization and the calculations of the electronic structures were performed by using the VASP code.[26,27] The projector augmented-wave pseudopotentials

https://doi.org/10.1021/acs.chemmater.2c02748
Chem. Mater. 2022, 34, 10068−10076

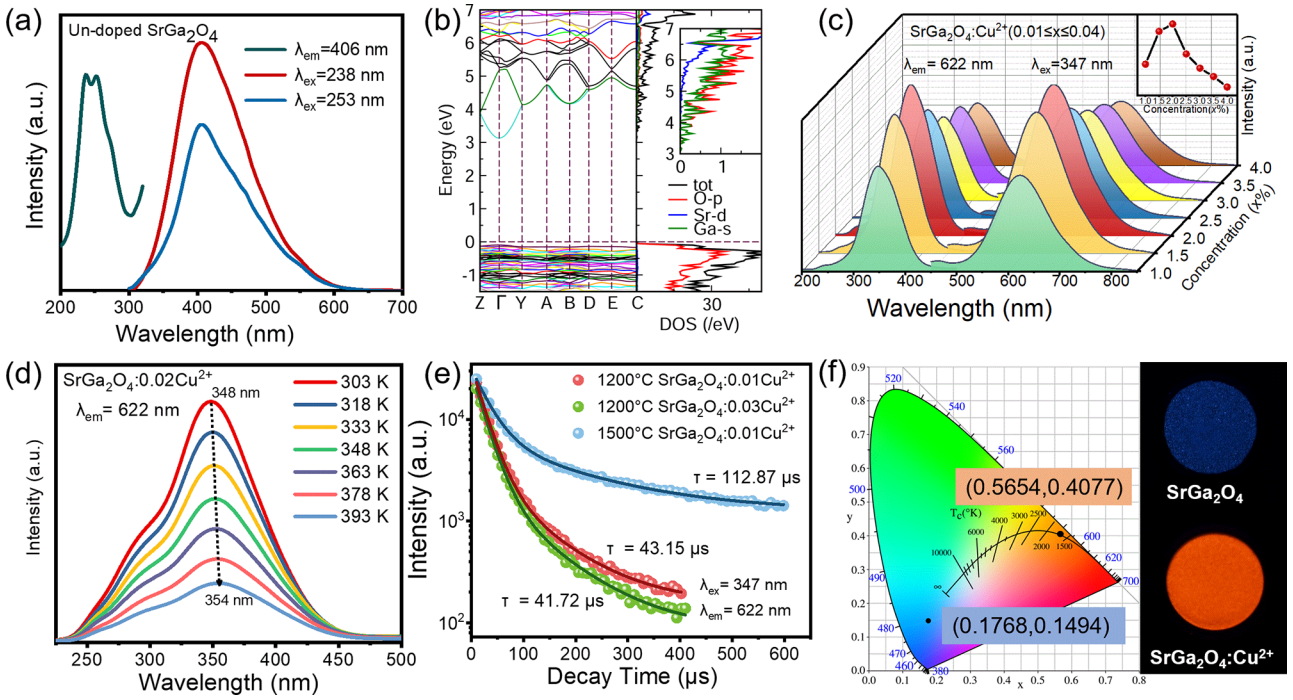

Figure 2. Excitation and emission spectra of (a) $SrGa_2O_4$ and (c) $SrGa_2O_4$:xCu^{2+} (x = 0.01, 0.015, 0.02, 0.025, 0.03, 0.035, and 0.04). The inset in (c) shows the dependence of the integral emission intensity on the concentration of Cu ions (x). (b) Electronic structure of $SrGa_2O_4$ without Cu^{2+} dopant or intrinsic defects. The inset is the enlarged density of states for the bottom of the host conduction band. (d) Temperature dependence of excitation spectra for the $SrGa_2O_4$:$0.02Cu^{2+}$ phosphor. (e) Luminescence decay curves of $SrGa_2O_4$:xCu^{2+} (x = 0.01 and 0.03) sintered at 1200 °C and $SrGa_2O_4$:$0.01Cu^{2+}$ sintered at 1500 °C. (f) Chromaticity coordinate diagrams (CIE) of luminescent $SrGa_2O_4$ and $SrGa_2O_4$:$0.02Cu^{2+}$ and their photographs.

and the generalized gradient approximation (GGA) within the Perdew–Burke–Ernzerhof (PBE) exchange–correlation functional was adopted.[28] The energy cutoff of the plane-wave basis set was 400 eV. The structural model of the undoped $SrGa_2O_4$ was constructed by a primitive unit cell, and the optimized lattice constant parameters a, b, c, and β were 8.30, 8.97, 10.70 nm, and 93.89°, respectively. The defective structures were modeled by substituting one of the Sr atoms by a Cu atom or by removing one of the Sr, Ga, or O atoms (Sr vacancy, V_{Sr}; Ga vacancy, V_{Ga}; or O vacancy, V_O) from $SrGa_2O_4$. The Brillouin-zone integrations were performed on a 4 × 4 × 4 Γ-centered k-point mesh.

3. RESULTS AND DISCUSSION

XPS was used to characterize the valence state of copper in phosphors. As shown in Figure 1a, the peaks located at 932.9 and 953.3 eV can be assigned to the $2p_{3/2}$ and $2p_{1/2}$ core levels of Cu^{2+}, respectively, with the spin orbit splitting of 20.4 eV.[29,30] Moreover, the two strong satellite peaks around 942.6 and 960.0 eV clearly prove that the valence state of copper in $SrGa_2O_4$ is divalent.[31]

The XRD patterns of undoped $SrGa_2O_4$ and Cu^{2+}-doped samples $Sr_{1-x}Ga_2O_4$:xCu^{2+} (x = 0.01, 0.02, 0.03, and 0.04) are shown in Figure 1b. In this compound, GaO_4 tetrahedra connect with each other through the vertex-sharing O^{2-}. The Sr^{2+} ions locate in the interstitials of GaO_4 tetrahedra with two different sites, namely eightfold- and sevenfold-coordinated Sr1 and Sr2 sites, as denoted by green and yellow balls, respectively, in Figure 1c. The Rietveld crystal structure refinements were carried out on the XRD data of $SrGa_2O_4$:$0.02Cu^{2+}$ by taking the crystallographic data of ICSD no 72-0222 as the standard, and no impurities were found in $SrGa_2O_4$:Cu^{2+} phosphor, as shown in Figure 1d. In order to identify the possible incorporation position of Cu^{2+}, we examined the XRD patterns of samples with a variety of Cu^{2+} concentrations. With the rising Cu^{2+} concentration, we found the XRD peaks slightly shifted toward larger 2θ angles with respect to the pure $SrGa_2O_4$ lattice, as shown in Figure 1b, indicating the shrinkage of the host lattice. As the ionic radius of Cu^{2+} ($r(Cu^{2+})$ = 0.73 Å) is much smaller than that of Sr^{2+} ($r(Sr^{2+})$ = 1.13 Å) and larger than that of Ga^{3+} ($r(Ga^{3+})$ = 0.47 Å) ions,[32] the contraction of the unit cell possibly indicates the Cu^{2+} ions that tend to occupy the Sr^{2+} sites. The formation energies of Cu ions of 2+ and 1+ states are calculated, and the results show that Cu^{2+} is more stable than Cu^{+} in $SrGa_2O_4$. The detailed results together with the local environments of Cu^{2+} are described in the Supporting Information.

The DRS spectra of $SrGa_2O_4$ along with the different Cu concentrations of $SrGa_2O_4$:xCu^{2+} are exhibited in Figure 1e. The host absorption edge starts from 280 nm, implying that the relevant band gap is about 5.15 eV, estimated with the well-known Kubelka–Munk formula[33] and Tauc relationship,[34,35] which is consistent with the value of 5.25 eV reported in ref 21. When Cu ions are doped in the host lattice, the absorption profile is well retained with Cu concentration, and three bands could be observed. The band around 340 nm might originate from the charge-transfer transition from O^{2-} to Cu^{2+}, analogous to the charge-transfer absorption in the range of 300–400 nm for $Na_2ZnP_2O_7$.[36] The band at 740 nm can be attributed to the d–d transition of Cu^{2+}, similar to Cu^{2+} in compounds with weak crystal fields.[13−17] Further analysis about the charge-transfer band is discussed below. Besides, the absorption band at 510 nm may be caused by the unknown species of defect introduced by the doped Cu^{2+} ions.

https://doi.org/10.1021/acs.chemmater.2c02748
Chem. Mater. 2022, 34, 10068−10076

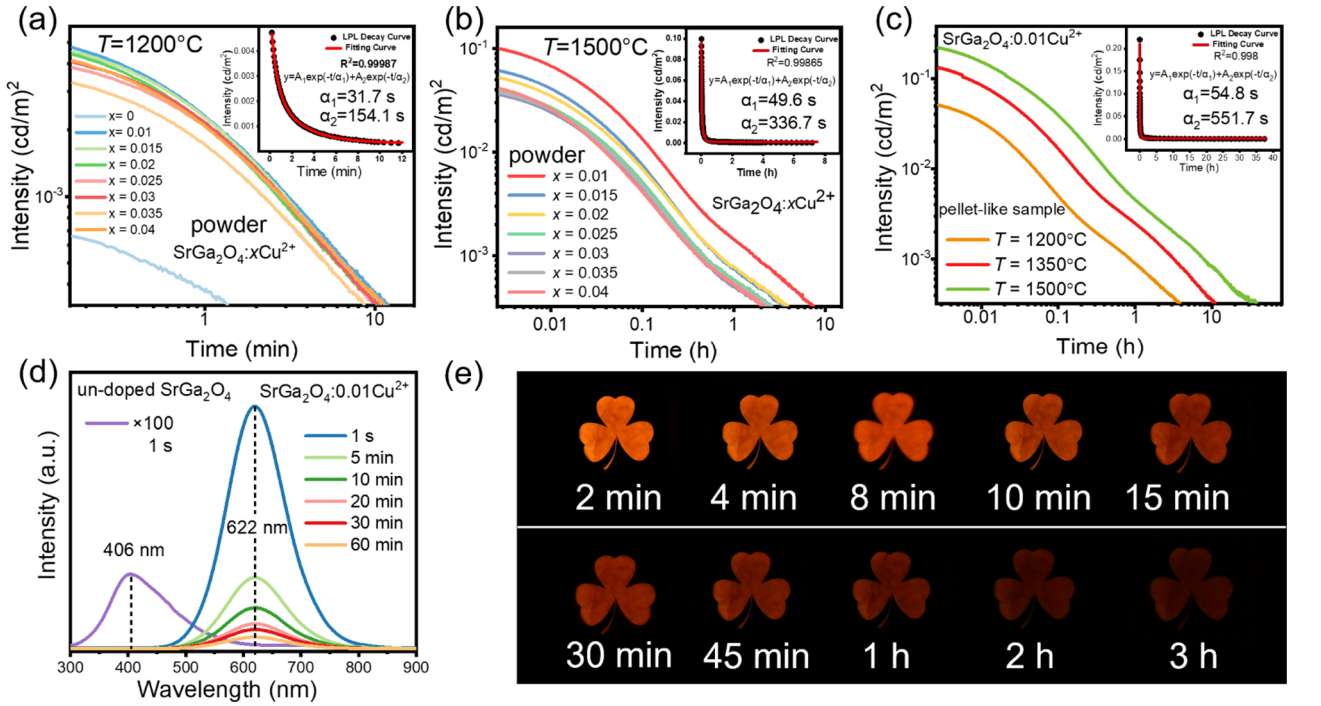

Figure 3. LPL decay curves of $SrGa_2O_4$:xCu^{2+} (x = 0, 0.01, 0.015, 0.02, 0.025, 0.03, 0.035, and 0.04) powder samples sintered at (a) 1200 and (b) 1500 °C after excitation for 30 min by 254 nm light for x = 0 and 365 nm light for others. The inset shows the exponentially fitting decay curves, with the Cu^{2+} concentration of 1%. (c) LPL decay curves of the pellet-like sample with sintered temperature from 1200 to 1500 °C after 365 nm excitation for 30 min. (d) LPL emission spectra of undoped $SrGa_2O_4$ (powder sample) and $Sr_{0.99}Ga_2O_4$:$0.01Cu^{2+}$ (pellet-like sample sintered at 1500 °C) recorded at different times after 365 nm excitation for 30 min. (e) LPL photographs of $SrGa_2O_4$:$0.01Cu^{2+}$ (pellet-like sample sintered at 1500 °C) taken at different times after removing the excitation source.

The excitation and emission spectra of undoped $SrGa_2O_4$ are shown in Figure 2a. Monitored at 406 nm, the excitation spectrum exhibits two adjacent narrow bands peaking at 238 and 253 nm, which are consistent with the DRS spectra in Figure 1e and virtually ascribed to the host excitation. Under the excitation of 238 or 253 nm, a broad emission band peaking at 406 nm can be observed. To further understand this excitation−emission process, we calculated the electronic structure of undoped $SrGa_2O_4$ by using the first-principles calculation, and the result is shown in Figure 2b. Both the valence band maximum (VBM) and the conduction band minimum (CBM) locate at the Γ point of the Brillouin zone, and the band gap predicted at the GGA-PBE level for $SrGa_2O_4$ is about 3.22 eV, which is about 1.93 eV lower than the experimental one as the GGA−PBE calculation usually underestimates the band gap. From the total and partial density of states (TDOS and PDOS), as shown in Figure 2b, it is observed that the valence band near the band gap is mostly from the O 2p states, while the lower conduction band comes from the hybridization between O 2p states, Ga 3s states, and Sr 4d states. Therefore, the emission of undoped $SrGa_2O_4$ is largely attributed to the self-excitation of GaO_4 tetrahedron.

When Cu^{2+} ions are introduced into $SrGa_2O_4$, they are excited by UV light from 280 to 420 nm, with the maximum at 347 nm and a shoulder at about 280 nm, as shown in Figure 2c. From the comparison with undoped $SrGa_2O_4$, the shoulder can be assigned to the excitation of the host. We associate the peak at 347 nm with the electronic transition from O^{2-} ion to Cu^{2+} ion, that is, the charge transfer band of O^{2-}−Cu^{2+}. When increasing the temperature, this excitation peak shifts to a longer wavelength, as shown in Figure 2d, which is the primary feature of the charge-transfer band. By the way, the excitation peaks of the Cu^{2+} d−d transitions are always located in the range from red to near infrared light.[13−17]

The emission spectra of $SrGa_2O_4$:Cu^{2+} are also shown in Figure 2c, where a red broad emission band with the maximum at about 622 nm can be observed. The full width at half-maximum of this emission peak is about 150 nm. Generally, the d−d transition of Cu^{2+} in almost all the phosphors reported produces an infrared emission, as the crystal field felt by Cu^{2+} ion is usually weak.[13−17] Cu^{2+} ions with $3d^9$ configuration could accommodate only one additional electron in order to fill up the 3d orbitals. Hence, the electron transferring from the O^{2-} ion can fully occupy the 3d levels of Cu^{2+} for the charge-transfer process. In this situation, the excited Cu ion releases its excited energy through electron transition from d levels to O ion, which we can name as the charge-transfer emission. Considering the distribution of Cu^{2+}, as mentioned in the Supporting Information, the broad emission peak may be due to the overlap of Cu^{2+} in both Sr sites. The integral emission intensity curve versus the content of Cu^{2+} is shown in the inset of Figure 2c, which implies that the optimal content of Cu^{2+} ions is about 2 mol % of Sr ions.

Figure 2e presents the luminescence decay curves of $SrGa_2O_4$:xCu^{2+} (x = 0.01 and 0.03) (λ_{ex} = 347 nm and λ_{em} = 622 nm) samples sintered at 1200 °C, which can be fitted well by a double exponential formula[37]

$$I = A_0 + A_1 \exp\left(-\frac{t}{\tau_1}\right) + A_2 \exp\left(-\frac{t}{\tau_2}\right)$$

where I represents the luminescence intensity, and A_0, A_1, and A_2 are constants. τ_1 and τ_2 are the luminescence lifetimes, from which the average decay time can be calculated by using the

https://doi.org/10.1021/acs.chemmater.2c02748
Chem. Mater. 2022, 34, 10068−10076

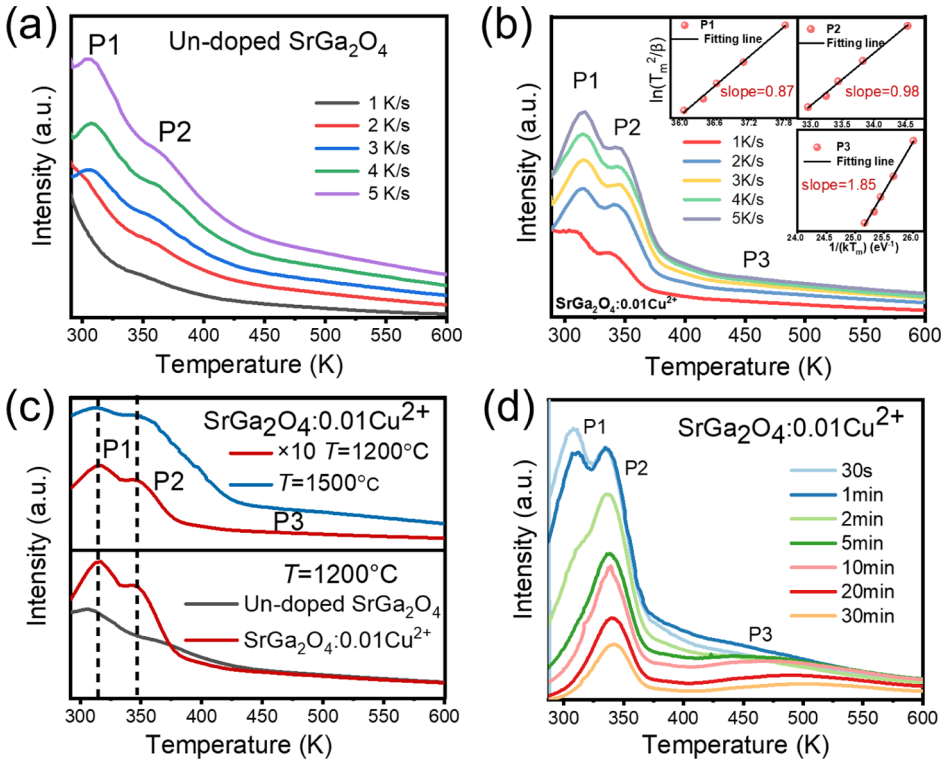

Figure 4. TL curves of $SrGa_2O_4$ (a) and $SrGa_2O_4$:0.01Cu^{2+} (b) recorded immediately after an irradiation of 365 nm for 30 min. The insets show the relationships between $\ln(T_m^2/\beta)$ and $1/kT_m$. (c) TL curves of $SrGa_2O_4$ and $SrGa_2O_4$:0.01Cu^{2+} at different sintering temperatures. (d) TL curves of $SrGa_2O_4$:0.01Cu^{2+} measured at different decay times after the removal of the UV lamp.

formula $\tau_{avg} = (A_1\tau_1^2 + A_2\tau_2^2)/(A_1\tau_1 + A_2\tau_2)$. It can be observed that the average decay time of $SrGa_2O_4$:0.03Cu^{2+} is 41.3 μs, which is shorter than that of $SrGa_2O_4$:0.01Cu^{2+} of 43.2 μs. This may be due to the concentration quenching from energy transfer. Figure 2e also shows the decay curve of $SrGa_2O_4$:0.01Cu^{2+} sintered at 1500 °C; the decay time is quite longer. This may be due to the higher quality of crystallization of the host and lower energy-transfer probability from Cu^{2+} to the quenching centers.

From the emission spectra in Figure 2c, the chromaticity coordinates of $SrGa_2O_4$:0.02Cu^{2+} are estimated to be (0.57, 0.41) by the chromaticity coordinate calculation, indicated in the red range of the Commission Internationale de l'Enclairage (CIE) chromaticity diagram shown in Figure 2f. For comparison, the chromaticity coordinates of undoped $SrGa_2O_4$ are indicated. On the right side are the photographs of the luminescent $SrGa_2O_4$ and $SrGa_2O_4$:0.02Cu^{2+} when excited with UV lamps.

The process of charge transfer from the ligand O^{2-} ion to Cu^{2+} ion could be simulated by the optical transition level (OTL),[38,39] which is the energy needed for an electron at the VBM to transition to the lowest empty 3d state of Cu^{2+}. The OTL is defined as shown in the Supporting Information, and the calculated OTL(Cu^{2+}) is about 2.74 eV on the Sr1 site and 2.46 eV on the Sr2 site, roughly in agreement with the experimental result (3.57 eV), considering the calculated OTL always systematically underestimates the experimental charge-transfer energies by about 1 eV.[38]

Then, we discuss the long persistent luminescence (LPL) of $Sr_{1-x}Ga_2O_4$:$x$$Cu^{2+}$ phosphors. The undoped $SrGa_2O_4$ produces LPL emission, peaking at 406 nm after the sample is exposed to 254 nm UV light for about 30 min. Its afterglow lasts about 2−3 min, as shown in Figure 3a. When doped with Cu^{2+} ions, the samples exhibit red LPL emission, with the maximum at about 622 nm rather than 406 nm, implying that the Cu^{2+} ions indeed could act as emission centers in the LPL process. The afterglow decay curves of $SrGa_2O_4$:$x$$Cu^{2+}$ (x = 0, 0.01, 0.015, 0.02, 0.025, 0.03, 0.035, and 0.04) powder samples sintered at 1200 °C are shown in Figure 3a. The initial luminance decreases fast, following the cease of excitation illumination, and then decreases very slowly. When the doping concentration is 1%, the sample has the strongest initial LPL intensity, and the decay can last more than 12 min before a LPL luminance of 0.32 mcd/m^2 is reached. The afterglow curve fitted by the double-exponential decay equation shows that the lifetime of the rapid decay is 31.7 s and that of the slow decay is 154 s.

After we increased the sintering temperature to 1500 °C in the preparation of $Sr_{1-x}Ga_2O_4$:$x$$Cu^{2+}$ (x = 0, 0.01, 0.015, 0.02, 0.025, 0.03, 0.035, and 0.04), we find that its afterglow can be dramatically prolonged to over 8 h (Figure 3b). The afterglow can be further extended to 36 h after the sample is compacted into a pellet-like sample with an additional sinter treatment at 1500 °C for 6 h (Figure 3c). The lifetimes of the rapid and slow decays are increased up to 54.8 and 551.7 s, respectively. Figure 3d shows the emission spectra of the pellet-like sample $SrGa_2O_4$:0.01Cu^{2+} captured at different decay times in the first 1 h of its afterglow process. The profiles of the emission spectra do not change with time, indicating that the red persistent luminescence originates from the Cu^{2+} emitting centers. Figure 3e shows the LPL photographs of the pellet-like sample $SrGa_2O_4$:0.01Cu^{2+} with red emission at different times. Its afterglow emission can be still observed after 3 h. After 36 h, the red light could be still detected beyond 0.32 mcd/m^2.

https://doi.org/10.1021/acs.chemmater.2c02748
Chem. Mater. 2022, 34, 10068−10076

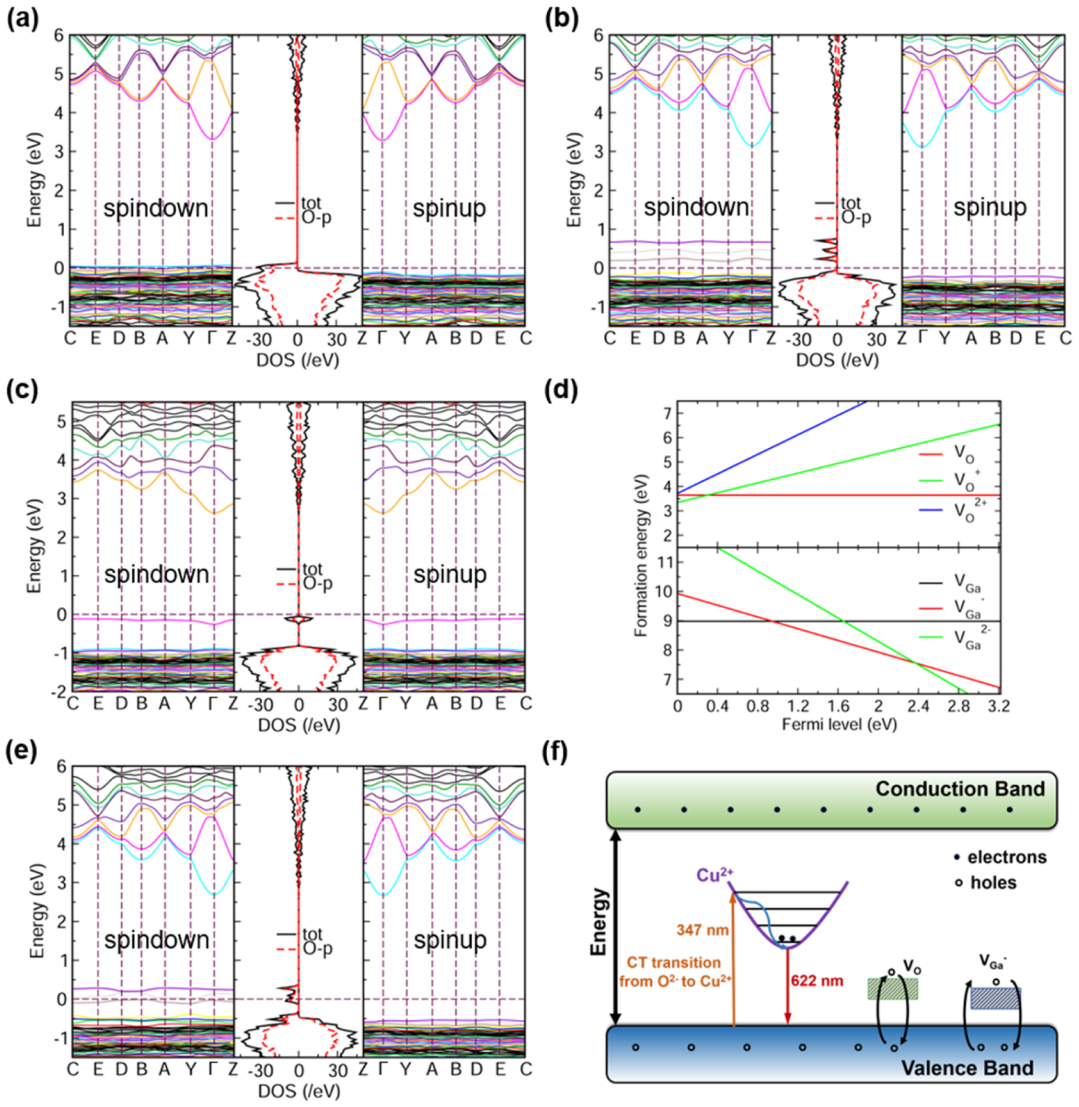

Figure 5. Band structures, TDOS, and PDOS of $SrGa_2O_4$ with (a) V_{Sr}, (b) V_{Ga}, (c) V_O, and (e) V_{Ga}^-. (d) Calculated formation energies of V_O and V_{Ga} in different charge states as a function of the energy of the Fermi level. (f) Illustration of the LPL mechanism of $SrGa_2O_4$:Cu^{2+}.

This means that the red-color-emitting $SrGa_2O_4$:Cu^{2+} LPL phosphors, to some extent, are comparable with the current commercial $SrAl_2O_4$:Eu, Dy LPL phosphors and might have wide potential applications in practice.

To explore the underlying LPL mechanism, the TL curves of $SrGa_2O_4$ and $Sr_{0.99}Cu_{0.01}Ga_2O_4$, shown in Figure 4a,b, are observed. For the undoped $SrGa_2O_4$, there are two quite weak peaks located at P1 (308 K) and P2 (367 K), which may be due to the trap levels induced by the intrinsic defects. The introduction of the Cu^{2+} ion in $SrGa_2O_4$ has little influence on the positions of these two peaks but drastically enhances their intensities (shown in the lower panel of Figure 4c). This indicates that the doping of Cu^{2+} ions will increase the concentration of the intrinsic defects and subsequently enhance the luminance of the afterglow and significantly prolong the decay time. Notably, these two peaks are close to the ambient temperature and are dominantly effective for the performance of the afterglow. Then, we estimate the trap level depths of these two peaks based on the equation $\frac{\beta E}{kT_m^2} = s\exp\left(-\frac{E}{kT_m}\right)$.[40] β is the heating rate; k is the Boltzmann constant (eV/K); T_m is the peak temperature (K) of the glow curve; E is the energy of the trap depth; and s is the frequency factor. The fitting result between $\ln(T_m^2/\beta)$ and $1/kT_m$ yields a straight line, as exhibited in Figure 4b. The depths of these two trap levels are estimated to be about 0.87 and 0.98 eV, respectively. For the $SrGa_2O_4$:$0.01Cu^{2+}$ powder sample sintered at 1500 °C, its TL curve is shown in Figure 4c together with that at 1200 °C for comparison. It is found that a higher sintering temperature could further enhance the peak intensities in the TL curve but hold the same positions. Notably, the crystal structure of the sample sintered at 1500 °C is totally the same as that sintered at 1200 °C, as shown in Figure 1b. This result implies that the increase of the sintering temperature might possibly increase the concentration of the intrinsic defects serving as the carrier-trapping centers.

To further understand the role of these trap levels, we sought to collect the TL curves of $SrGa_2O_4$:$0.01Cu^{2+}$ for various decay times to observe the carrier-release behavior. As shown in Figure 4d, the P1 peak decays very quickly and is nearly absent in 4 min after ceasing the irradiation, implying that the energy stored in the trap level P1 first releases to sustain the emission of Cu^{2+} ions. The P2 peak keeps its intensity without any significant change in the initial first

https://doi.org/10.1021/acs.chemmater.2c02748
Chem. Mater. 2022, 34, 10068−10076

minute; subsequently, its intensity gradually decreases with the decay time and does not disappear after 30 min. The mid-term LPL phenomenon of $SrGa_2O_4:Cu^{2+}$ should be dominantly attributed to this trap level. It is worth noting that when the intensities of traps P1 and P2 decrease, the peak of trap P3 gradually emerges. The trap levels corresponding to the P3 peak have a depth of about 1.85 eV. As the intensity of the trap P2 decreases gradually and the trap P3 begins to take effect, the decay enters a slow decay process. In a word, the incorporation of Cu^{2+} ions boosts the creation of appropriate trap levels and makes a significant influence on the LPL performance.

To understand the LPL mechanism, it is necessary to clear the specific types of defects playing the key role in the LPL process. We focus on the intrinsic defects such as Sr vacancy (V_{Sr}), Ga vacancy (V_{Ga}), and O vacancy (V_O), as no foreign dopants were introduced into the $SrGa_2O_4$ lattice except for Cu ions. The calculated electronic structures with both spin-up and spin-down states (Figure 5a) show that V_{Sr} could not bring in any defect levels in the band gap, but could induce holes at the VBM, as some states near VBM are above the Fermi level. Figure 5b exhibits the electronic structure of V_{Ga}, where three spin-down defect levels appear at about 0.3, 0.6, and 0.8 eV above the VBM. The PDOS exhibit that these defect levels originate from the 2p orbitals of O^{2-} ions surrounding V_{Ga}. All these defect levels are empty as they are above the Fermi level and hence might accommodate electrons with their charge state changing from 0 to −1 or −2 (denoted as V_{Ga}^{-} or V_{Ga}^{2-}). Figure 5c shows the electronic structure of V_O, where a fully occupied defect level appears at about 0.9 eV above the VBM. The electrons in this defect level could be excited to the conduction band or transfer to the valence band if holes exist in the valence band, leaving V_O in +1 or +2 charge state (V_O^{+} or V_O^{2+}). In other words, V_O could serve as a hole-trapper.

From the analysis above, we can see that both Ga and O vacancies may be in different charge states. Therefore, it is essential to compute the formation energies of V_{Ga} or V_O in these charge states to compare their relative stabilities by using the following formula

$$E_F(V_X^{n+}) = E^n(V_X) - E(SrGa_2O_4) - \mu(X) + n\varepsilon_f$$

where X represents Ga or O. $E_F(V_X^{n+})$ is the formation energy of X vacancy, with the charge state of $n+$. $E^n(V_X)$ is the total energy of $SrGa_2O_4$ containing a $n+$ charged X vacancy. $\mu(X)$ is the chemical potential of the bulk Ga or O_2 molecule in a vacuum, and ε_f is the Fermi level of the system. The calculated formation energies of V_O, V_O^{+}, and V_O^{2+} versus the energies of the Fermi level are shown in Figure 5d. The Fermi level changes from the VBM (taken as the reference) to the CBM. When the Fermi level is higher than 0.3 eV, V_O has the lowest formation energy and so is most stable. V_O^{+} becomes more stable when the Fermi level is below 0.3 eV, while V_O^{2+} hardly exists as it has the highest formation energy in the complete Fermi-level range. Considering the calculated band gap is only 3.22 eV, the Fermi level at 0.3 eV is very close to the VBM, implying most O vacancies existing in $SrGa_2O_4$ are electronically neutral.

Figure 5d shows the formation energies of V_{Ga}, V_{Ga}^{-}, and V_{Ga}^{2-} versus the Fermi level. The neutral Ga vacancy is only stable when the Fermi level is lower than 0.94 eV, and V_{Ga}^{2-} becomes more stable when the Fermi level is higher than 2.37 eV. When the Fermi level is in between, V_{Ga}^{-} is more stable. In the $SrGa_2O_4$ sample, the Fermi level should be close to the middle of the band gap, as no donor or acceptor impurities have been doped. Thus, the Ga vacancies in $SrGa_2O_4$ should reasonably be in −1 state. The electronic structure of V_{Ga}^{-} is very similar to that of V_{Ga}, except that an electron occupies the defect levels, as shown in Figure 5e. Hence, the hole at the valence band could be trapped in V_{Ga}^{-}. The trap levels observed in the TL curves, as shown in Figure 4, can be probably ascribed to V_{Ga}^{-} and V_O.

We can describe the LPL mechanism of $SrGa_2O_4:Cu^{2+}$ based on the calculated defect levels summarized in Figure 5f. When excited by 347 nm light, the electrons at the O^{2-} ions at about the top of the valence band transfer to the 3d levels of Cu^{2+} ions, leaving holes at the valence band, as shown by the orange arrow. These excited electrons (at Cu^{2+}) can recombine with the holes (in the valence band), resulting in the red emission. Such recombination can be continued after stopping the excitation if the holes are trapped by the defect levels that are induced by V_{Ga}^{-} or V_O and then thermally released back to the valence band, resulting in an afterglow. When the sample is prepared at 1500 °C, more O and Ga atoms could escape from the host, resulting in more V_{Ga}^{-} and V_O defects, and consequently the afterglow will be enhanced.

4. CONCLUSIONS

In conclusion, we have developed a new type of red-emitting phosphor $SrGa_2O_4:Cu^{2+}$ synthesized by a high-temperature solid-state reaction method, and its persistent luminescence properties were studied. A broad excitation band peaking at 347 nm and a broad emission band at 622 nm are observed, which are attributed to the electron transfer between the O^{2-} ion and the Cu^{2+} ion. The afterglow decay time of $SrGa_2O_4:Cu^{2+}$ could last over 36 h, which is much longer than that of the present widely used red-emitting LPL materials reported in the literature and even comparable with the current commercial blue-/green-emitting LPL phosphors. Combining the TL measurement and the first-principles calculation, we find that both the O vacancy and −1 charged Ga vacancy have suitable trap depths and could trap holes from the valence band, remarkably delay the emission process after stopping the excitation, and produce the afterglow. Our findings here may motivate further research works on the invention of lanthanide-ion-free Cu^{2+}-activated phosphors and provide new opportunities for the development of multicolor LPL materials and applications.

■ ASSOCIATED CONTENT

Supporting Information

The Supporting Information is available free of charge at https://pubs.acs.org/doi/10.1021/acs.chemmater.2c02748.

Stabilities of Cu^{2+} and Cu^{+} in $SrGa_2O_4$; structural information of Cu^{2+} in $SrGa_2O_4$; and OTL of Cu^{2+} in $SrGa_2O_4$ (PDF)

■ AUTHOR INFORMATION

Corresponding Authors

Bingyan Qu − *School of Materials Science and Engineering, Hefei University of Technology, Hefei, Anhui 230009, P. R. China;* orcid.org/0000-0002-1676-7586; Email: byqu@hfut.edu.cn

https://doi.org/10.1021/acs.chemmater.2c02748
Chem. Mater. 2022, 34, 10068−10076

Hubertus T. Hintzen − *Fundamental Aspects of Materials and Energy, Delft University of Technology, Delft 2629 JB, Netherlands*; Email: H.T.Hintzen@tudelft.nl

Authors

Lei Wang − *School of Materials Science and Engineering, Hefei University of Technology, Hefei, Anhui 230009, P. R. China*; orcid.org/0000-0001-7428-2766

Cailu Wang − *School of Materials Science and Engineering, Hefei University of Technology, Hefei, Anhui 230009, P. R. China*

Yang Chen − *School of Materials Science and Engineering, Hefei University of Technology, Hefei, Anhui 230009, P. R. China*

Yang Jiang − *School of Materials Science and Engineering, Hefei University of Technology, Hefei, Anhui 230009, P. R. China*; orcid.org/0000-0002-5364-1421

Lei Chen − *School of Materials Science and Engineering, Hefei University of Technology, Hefei, Anhui 230009, P. R. China*; orcid.org/0000-0002-8045-6336

Jinzhang Xu − *School of Electrical Engineering and Automation, Hefei University of Technology, Hefei, Anhui 230009, P. R. China*

Complete contact information is available at: https://pubs.acs.org/10.1021/acs.chemmater.2c02748

Author Contributions

L.W. contributed to the design of experiments, calculations, result analysis, interpretation, and discussion and prepared the original manuscript. C.W. conducted the experiments, contributed to the result analysis and discussion, and prepared the original manuscript. Y.C. conducted the experiments. Y.J., L.C., and J.X. contributed to the result discussion. B.Q. contributed to the design of experiments, calculations, result analysis, interpretation, discussion, and prepared the original manuscript. H.T.H. contributed to the result analysis and discussion and prepared the original manuscript. This final version of the manuscript was critically reviewed and received approval from all authors.

Notes

The authors declare no competing financial interest.

■ ACKNOWLEDGMENTS

This work was supported by the Fundamental Research Funds for the Central Universities (JZ2020HGTB0036), the Natural Science Foundation of Anhui Province (1708085ME121), and the Industrial Innovation Guidance Fund of Tongcheng City & Hefei University of Technology (JZ2022YDZJ0083). Calculations were done in the Supercomputing Center of University of Science and Technology of China.

■ REFERENCES

(1) Li, W.; Zhuang, Y.; Zheng, P.; Zhou, T.-L.; Xu, J.; Ueda, J.; Tanabe, S.; Wang, L.; Xie, R.-J. Tailoring trap depth and emission wavelength in $Y_3Al_{5-x}Ga_xO_{12}$:Ce^{3+}, V^{3+} phosphor-in-glass films for optical information storage. *ACS Appl. Mater. Interfaces* **2018**, *10*, 27150−27159.

(2) Liu, F.; Yan, W.; Chuang, Y.-J.; Zhen, Z.; Xie, J.; Pan, Z. Photostimulated near-infrared persistent luminescence as a new optical read-out from Cr^{3+}-doped $LiGa_5O_8$. *Sci. Rep.* **2013**, *3*, 1554.

(3) Wang, W.; Yan, S.; Liang, Y.; Chen, D.; Wang, F.; Liu, J.; Zhang, Y.; Sun, K.; Tang, D. A red-light-chargeable near infrared $MgGeO_3$:Mn^{2+}, Yb^{3+} persistent phosphor for bioimaging and optical information storage applications. *Inorg. Chem. Front.* **2021**, *8*, 5149−5157.

(4) Li, Y.; Gecevicius, M.; Qiu, J. Long persistent phosphors - from fundamentals to applications. *Chem. Soc. Rev.* **2016**, *45*, 2090−2136.

(5) Pan, Z.; Lu, Y. Y.; Liu, F. Sunlight-activated long-persistent luminescence in the near-infrared from Cr^{3+}-doped zinc gallogermanates. *Nat. Mater.* **2011**, *11*, 58−63.

(6) Abdukayum, A.; Chen, J.-T.; Zhao, Q.; Yan, X.-P. Functional Near Infrared-Emitting Cr^{3+}/Pr^{3+} Co-Doped Zinc Gallogermanate Persistent Luminescent Nanoparticles with Superlong Afterglow for in Vivo Targeted Bioimaging. *J. Am. Chem. Soc.* **2013**, *135*, 14125−14133.

(7) Sun, S.-K.; Wang, H.-F.; Yan, X.-P. Engineering persistent luminescence nanoparticles for biological applications: From biosensing/bioimaging to theranostics. *Acc. Chem. Res.* **2018**, *51*, 1131−1143.

(8) Zhou, Z.; Zheng, W.; Kong, J.; Liu, Y.; Huang, P.; Zhou, S.; Chen, Z.; Shi, J.; Chen, X. Rechargeable and LED-activated $ZnGa_2O_4$:Cr^{3+} near-infrared persistent luminescence nanoprobes for background-free biodetection. *Nanoscale* **2017**, *9*, 6846−6853.

(9) Qu, B.; Zhang, B.; Wang, L.; Zhou, R.; Zeng, X. C. Mechanistic study of the persistent luminescence of $CaAl_2O_4$:Eu, Nd. *Chem. Mater.* **2015**, *27*, 2195−2202.

(10) Rojas-Hernandez, R. E.; Rubio-Marcos, F.; Rodriguez, M. Á.; Fernandez, J. F. Long lasting phosphors: $SrAl_2O_4$:Eu, Dy as the most studied material. *Renew. Sustain. Energy Rev.* **2018**, *81*, 2759−2770.

(11) Li, W.; Liu, Y.; Ai, P. Synthesis and luminescence properties of red long-lasting phosphor Y_2O_2S:Eu^{3+}, Mg^{2+}, Ti^{4+} nanoparticles. *Mater. Chem. Phys.* **2010**, *119*, 52−56.

(12) Hu, Y.; Zhuang, W.; Ye, H.; Zhang, S.; Fang, Y.; Huang, X. Preparation and luminescent properties of $(Ca_{1-x},Sr_x)S$:Eu^{2+} red-emitting phosphor for white LED. *J. Lumin.* **2005**, *111*, 139−145.

(13) Romanov, A. N.; Haula, E. V.; Shashkin, D. P.; Korchak, V. N. Broadband Near-IR photoluminescence of trigonal-bipyramidal coordinated Cu^{2+} impurity center in $YGaO_3$, $YInO_3$ and $GdInO_3$ hexagonal phases. *J. Lumin.* **2020**, *228*, 117652.

(14) Li, Y.-J.; Ye, S.; Wang, C.-H.; Wang, X.-M.; Zhang, Q.-Y. Temperature-dependent near-infrared emission of highly concentrated Cu^{2+} in $CaCuSi_4O_{10}$ phosphor. *J. Mater. Chem. C* **2014**, *2*, 10395−10402.

(15) Comelli, D.; Capogrosso, V.; Orsenigo, C.; Nevin, A. Dual wavelength excitation for the time-resolved photoluminescence imaging of painted ancient Egyptian objects. *Heritage Sci.* **2016**, *4*, 21.

(16) Szyszka, K.; Targońska, S.; Lewińska, A.; Watras, A.; Wiglusz, R. J. Quenching of the Eu^{3+} Luminescence by Cu^{2+} Ions in the Nanosized Hydroxyapatite Designed for Future Bio-Detection. *Nanomaterials* **2021**, *11*, 464.

(17) Dubicki, L.; Riley, M. J.; Krausz, E. R. Electronic structure of the copper(II) ion doped in cubic $KZnF_3$. *J. Chem. Phys.* **1994**, *101*, 1930−1938.

(18) Lee, D. J.; Lee, Y. S.; Noh, H. J. Multicolor tunable emission induced by Cu ion doping of perovskite zirconate. *J. Lumin.* **2016**, *169*, 128−131.

(19) Aidilibike, T.; Li, Y.; Guo, J.; Liu, X.; Qin, W. Blue upconversion emission of Cu^{2+} ions sensitized by Yb^{3+}-trimers in CaF_2. *J. Mater. Chem. C* **2016**, *4*, 2123−2126.

(20) Liu, S.; Ma, S.; Wang, S.; Ye, Z. Exploring crystal-field splittings of Eu^{3+} ions in γ- and β-$SrGa_2O_4$. *J. Lumin.* **2019**, *210*, 155−163.

(21) Cai, X.; Mu, Z.; Zhang, S.; Zhu, D.; Wang, Q.; Yang, Y.; Luo, D.; Wu, F. An investigation about the luminescence mechanism of $SrGa_2O_4$:Eu^{3+} showing no detectable energy transfer from the host to the dopant ions. *J. Lumin.* **2018**, *200*, 169−174.

(22) Bin, Q.; Zilong, T.; Zhongtai, Z.; Lei, C. Citric gel synthesis and luminescent properties of Ce^{3+}-activated $SrGa_2O_4$ Phosphor. *J. Rare Earths* **2007**, *25*, 286−290.

(23) Mondal, A.; Manam, J. Citrate sol-gel synthesis and luminescent properties of Cr^{3+}-activated strontium gallate phosphor. *AIP Conf. Proc.* **2019**, *2115*, 030193.

(24) Wang, T.; Xu, X.; Zhou, D.; Yang, Y.; Qiu, J.; Yu, X. Effect of defect distribution on the optical storage properties of strontium

gallates with a low-dimensional chain structure. *Inorg. Chem.* **2016**, *55*, 894−901.
(25) Yu, X.; Wang, S.; Zhu, Y.; Liang, J.; Qiu, J.; Xu, X.; Lu, W. High-temperature long persistent and photo-stimulated luminescence in Tb^{3+} doped gallate phosphor. *J. Alloys Compd.* **2017**, *701*, 774−779.
(26) Kresse, G.; Furthmüller, J. Efficient iterative schemes for ab initio total-energy calculations using a plane-wave basis set. *Phys. Rev. B: Condens. Matter Mater. Phys.* **1996**, *54*, 11169−11186.
(27) Kresse, G.; Hafner, J. Ab Initio molecular dynamics for liquid metals. *Phys. Rev. B: Condens. Matter Mater. Phys.* **1993**, *47*, 558−561.
(28) Perdew, J. P.; Burke, K.; Ernzerhof, M. Generalized Gradient Approximation Made Simple. *Phys. Rev. Lett.* **1996**, *77*, 3865−3868.
(29) Kong, C.; Tang, L.; Zhang, X.; Sun, S.; Yang, S.; Song, X.; Yang, Z. Templating synthesis of hollow CuO polyhedron and its application for nonenzymatic glucose detection. *J. Mater. Chem. A* **2014**, *2*, 7306−7312.
(30) Alam, M. M.; Asiri, A. M.; Uddin, M. T.; Inamuddin, I.; Islam, M. A.; Awual, M. R.; Rahman, M. M. One-step wet-chemical synthesis of ternary ZnO/CuO/Co_3O_4 nanoparticles for sensitive and selective melamine sensor development. *New J. Chem.* **2019**, *43*, 4849−4858.
(31) Qi, K.; Xing, X.; Zada, A.; Li, M.; Wang, Q.; Liu, S.-y.; Lin, H.; Wang, G. Transition metal doped ZnO nanoparticles with enhanced photocatalytic and antibacterial performances: Experimental and DFT studies. *Ceram. Int.* **2020**, *46*, 1494−1502.
(32) Shannon, R. Revised effective ionic radii and systematic studies of interatomic distances in halides and chalcogenides. *Acta Crystallogr., Sect. A: Cryst. Phys., Diffr., Theor. Gen. Crystallogr.* **1976**, *32*, 751−767.
(33) Dutta, S.; Som, S.; Priya, J.; Sharma, S. K. Band gap, CIE and trap depth parameters of rare earth molybdate phosphors for optoelectronic applications. *Solid State Sci.* **2013**, *18*, 114−122.
(34) Som, S.; Mitra, P.; Kumar, V.; Kumar, V.; Terblans, J. J.; Swart, H. C.; Sharma, S. K. The energy transfer phenomena and colour tunability in $Y_2O_2S:Eu^{3+}/Dy^{3+}$ micro-fibers for white emission in solid state lighting applications. *Dalton Trans.* **2014**, *43*, 9860−9871.
(35) Tauc, J.; Menth, A. States in the gap. *J. Non-Cryst. Solids* **1972**, *8−10*, 569−585.
(36) Kumar, B. V.; Vithal, M. Luminescence (M=Mn^{2+}, Cu^{2+}) and ESR (M=Gd^{3+}, Mn^{2+}, Cu^{2+}) of $Na_2ZnP_2O_7$: M. *Phys. B* **2012**, *407*, 2094−2099.
(37) Chen, X.; Xia, Z. Luminescence properties of $Li_2Ca_2ScV_3O_{12}$ and $Li_2Ca_2ScV_3O_{12}:Eu^{3+}$ synthesized by solid-state reaction method. *Opt. Mater.* **2013**, *35*, 2736−2739.
(38) Qu, B.; Zhou, R.; Wang, L.; Dorenbos, P. How to predict the location of the defect levels induced by 3d transition metal ions in octahedral sites of aluminate phosphors. *J. Mater. Chem. C* **2019**, *7*, 95−103.
(39) Van de Walle, C. G.; Neugebauer, J. First-principles calculations for defects and impurities: Applications to III-nitrides. *J. Appl. Phys.* **2004**, *95*, 3851−3879.
(40) Ueda, J.; Dorenbos, P.; Bos, A. J. J.; Kuroishi, K.; Tanabe, S. Control of electron transfer between Ce^{3+} and Cr^{3+} in the $Y_3Al_{5-x}Ga_xO_{12}$ host via conduction band engineering. *J. Mater. Chem. C* **2015**, *3*, 5642−5651.

https://doi.org/10.1021/acs.chemmater.2c02748
Chem. Mater. 2022, 34, 10068−10076